Universal quantum Otto heat machine based on the Dicke model

He-Guang Xu,[1] Jiasen Jin,[1,*] G. D. M. Neto,[2,†] and Norton G. de Almeida[3]
[1]*School of Physics, Dalian University of Technology, 116024 Dalian, China*
[2]*Department of Physics, Zhejiang Normal University, Jinhua 321004, China*
[3]*Instituto de Física, Universidade Federal de Goiás, 74.001-970, Goiânia, Goiás, Brazil*

(Received 13 August 2023; accepted 15 December 2023; published 18 January 2024)

In this paper we study a quantum Otto thermal machine where the working substance is composed of N identical qubits coupled to a single mode of a bosonic field, where the atoms and the field interact with a reservoir, as described by the so-called open Dicke model. By controlling the relevant and experimentally accessible parameters of the model we show that it is possible to build a universal quantum heat machine (UQHM) that can function as an engine, refrigerator, heater, or accelerator. The heat and work exchanges are computed taking into account the growth of the number N of atoms as well as the coupling regimes characteristic of the Dicke model for several ratios of temperatures of the two thermal reservoirs. The analysis of quantum features such as entanglement and second-order correlation shows that these quantum resources do not affect either the efficiency or the performance of the UQHM based on the open Dicke model. In addition, we show that the improvement in both efficiency and coefficient of performance of our UQHM occurs for regions around the critical value of the phase transition parameter of the model.

DOI: 10.1103/PhysRevE.109.014122

I. INTRODUCTION

Quantum thermodynamics [1–13], which is described by the laws of quantum mechanics and thermodynamics, plays a fundamental role in understanding the transitions between various forms of energy and has become a vibrant branch of modern research. A quantum heat engine (QHE) [4,14–22] is a quantum device to study the thermodynamic properties of quantum systems and generates power from the heat flow between hot and cold reservoirs. In recent years, the study of thermal nanomachines has been driven by the great theoretical and experimental effort dedicated to the investigation of their properties in the quantum regime. Nowadays, there are many experimental platforms to explore QHE, such as trapped ion systems [23–26], optomechanics [27,28], ultracold atoms [29,30], nuclear magnetic resonance (NMR) [31–33], and superconducting circuits [34–38].

Among thermal machines, great interest has been devoted to cyclic thermal machines, both refrigerators and engines, operating in the quantum regime where energy exchanges can occur, for example, between the reservoir and just two levels of a single atom or between levels of a quantum harmonic oscillator. Several typical quantum cycles have been extensively studied, such as Carnot, Otto, and Stirling cycles [4,12,13,20,39–47]. In this paper, we are only concerned with the quantum Otto cycle. The performance of the quantum Otto cycle depends strongly on the choice of the working substance. For example, recent studies show that, with two temperatures fixed, the Otto cycle performed with fermionic substances can surpass the performance of the same cycle when performed with bosonic substances [48]. Regarding the Otto cycle there are several cases being considered, such as single spin systems [49,50], two-level atoms [22], coupled spin systems [40,51,52], coupled spin-3/2 [53], harmonic oscillators [23,54], relativistic oscillators [55], Bose-Einstein condensates [56,57], and light-matter systems described by the Jaynes-Cumming [58–61] and quantum Rabi [62–67] models.

Despite the several studies on light-matter systems, there are very few works devoted to investigating a quantum Otto heat engine operating with multiqubits interacting with a single cavity mode in the dressed picture and taking into account dissipation as well as the number of two-level atoms, as described by the open Dicke model (ODM). Over the past decades, the Dicke model has been theoretically studied in several contexts, as for example quantum phase transition [68–76], quantum entanglement [77–79], chaos [80], lasing [81], and quantum thermodynamics [82]. According to the qubit-photon coupling ratio λ/ω, where λ is the coupling strength and ω is the frequency of the cavity mode field, the ODM can be divided into different coupling regimes: weak and strong coupling regime ($\lambda/\omega < 0.1$), ultrastrong coupling regime (USC) ($0.1 \leqslant \lambda/\omega < 1$), which was experimentally realized in a variety of quantum systems [83–91], and deep strong coupling regime (DSC) ($1 \leqslant \lambda/\omega$).

In this work, we study a quantum Otto heat machine (QOHM) operating under two thermal reservoirs and having as a working substance N atoms and one mode of an electromagnetic field, as modeled by the ODM. We calculate the total work extracted and the amount of heat exchanged between the system and the reservoir and both the efficiency of the engine and the coefficient of performance (COP) of the refrigerator by numerically solving the ODM using the extended bosonic coherent state approach and the dressed master

*jsjin@dlut.edu.cn
†gdmneto@zjnu.edu.cn

equation, which is suitable for any coupling strength regime to describe the ODM dynamics [92–96]. As we will show, it is possible, by controlling the ODM parameters, to build a universal quantum thermal machine [97] that, depending on the choice of parameters, can work either as an engine or as a refrigerator or as heater or as an accelerator. Furthermore, our results indicate that it is not possible, for the model analyzed here, to use quantum resources to improve the engine efficiency or the refrigerator performance.

This paper is organized as follows. In Sec. II we introduce the open Dicke model and numerically solve it by using the extended bosonic coherent state approach. In Sec. III we present our model for a universal QOHM, having as the working substance N two-level atoms and one mode of the electromagnetic field, with both atoms and field interacting with their respective reservoirs through the so-called open Dicke model. In Sec. IV, we study the roles of the qubit-mode coupling strength, the number N of qubits, and the temperature ratio between the cold and hot thermal reservoirs on the amount of work and heat extractable as well as the impact on the engine efficiency and the refrigerator performance when varying the system parameters. Finally, in Sec. V we present our conclusions.

II. MODEL

The Hamiltonian describing the Dicke model consisting of a single bosonic field interacting with N identical two-level qubits is expressed as ($\hbar = 1$) [98,99]

$$\hat{H}_0 = \omega_0 \hat{a}^\dagger \hat{a} + \Delta \hat{J}_z + \frac{2\lambda}{\sqrt{N}}(\hat{a}^\dagger + \hat{a})\hat{J}_x, \tag{1}$$

where ω_0 and Δ are the frequencies of the single bosonic mode and qubits, respectively, λ is the qubit-boson coupling strength, $\hat{a}^\dagger(\hat{a})$ denotes the creation (annihilation) operator of the bosonic field, $\hat{J}_x = \frac{1}{2}(\hat{J}_+ + \hat{J}_-)$ and $\hat{J}_z$ are the pseudospin operators given by $\hat{J}_\pm = \sum_i {}^N\hat{\sigma}_\pm{}^i$, $\hat{J}_z = \sum_i {}^N\hat{\sigma}_z{}^i$, with $\hat{\sigma}_\alpha$ ($\alpha = x, y, z$) being the Pauli operators. The pseudospin operators satisfy the commutation relation $[\hat{J}_+, \hat{J}_-] = 2\hat{J}_z$, $[\hat{J}_z, \hat{J}_\pm] = \pm\hat{J}_\pm$.

The Dicke model has a numerically exact solution by using an extended bosonic coherent state approach [75,76]. For convenience of numerical solution, we first rotate the angular momentum operators with $\pi/2$ along the y-axis $\hat{H}_s = \exp(i\pi\hat{J}_y/2)\hat{H}_0\exp(-i\pi\hat{J}_y/2)$, resulting in

$$\hat{H}_s = \omega_0\hat{a}^\dagger\hat{a} - \frac{\Delta}{2}(\hat{J}_+ + \hat{J}_-) + \frac{2\lambda}{\sqrt{N}}(\hat{a}^\dagger + \hat{a})\hat{J}_z. \tag{2}$$

For the two-level qubits, its basis can be spanned by the Dicke state $\{\{|j, m\rangle, m = -j, -j+1, \ldots, j-1, j\}$ with $j = N/2$ and the Hilbert space of the total system can be expressed in terms of the basis $\{|\varphi_m\rangle_b \otimes |j, m\rangle\}$. In the Dicke model, the excitation number $\hat{N} = \hat{a}^\dagger\hat{a} + \hat{J}_z + N/2$ is not conserved. Therefore, the truncation of the bosonic excitation number procedure has to be applied in this system, especially in the strong qubit-boson coupling regime. By considering the displacement transformation $\hat{A}_m = \hat{a} + g_m$ with $g_m = 2\lambda m/\omega\sqrt{N}$ and taking the total system basis into the Schrödinger equation, we obtain

$$\begin{aligned} &-\Delta j_m^+|\varphi_m\rangle_b|j, m+1\rangle - \Delta j_m^-|\varphi_m\rangle_b|j, m-1\rangle \\ &+\omega_0\big(\hat{A}_m^\dagger\hat{A}_m - g_m^2\big)|\varphi_m\rangle_b|j, m\rangle = E|\varphi_m\rangle_b|j, m\rangle, \end{aligned} \tag{3}$$

where $\hat{J}_\pm|j, m\rangle = j_m^\pm|j, m\pm1\rangle$, with $j_m^\pm = \sqrt{j(j+1) - m(m\pm1)}$. Next, we multiply Eq. (3) on the left by $\{\langle n, j|\}$, which results in

$$\begin{aligned} &-\Delta j_n^+|\varphi_{n+1}\rangle_b - \Delta j_n^-|\varphi_{n-1}\rangle_b + \omega_0\big(\hat{A}_n^\dagger\hat{A}_n - g_n^2\big)|\varphi_n\rangle_b \\ &= E|\varphi_n\rangle_b, \end{aligned} \tag{4}$$

where $n = -j, -j+1, \ldots, j$. Furthermore, the bosonic state can be expanded as

$$\begin{aligned} |\varphi_m\rangle_b &= \sum_{k=0}^{N_{\rm tr}} \frac{1}{\sqrt{k!}} c_{m,k}(\hat{A}_m^\dagger)^k|0\rangle_{A_m} \\ &= \sum_{k=0}^{N_{\rm tr}} \frac{1}{\sqrt{k!}} c_{m,k}(\hat{a}^\dagger + g_m)^k e^{-g_m\hat{a}^\dagger - g_m^2/2}|0\rangle_a, \end{aligned} \tag{5}$$

where $N_{\rm tr}$ is the truncation number of bosonic excitations. Finally, we obtain the eigenvalue equation

$$\begin{aligned} &\omega_0\big(l - g_n^2\big)c_{n,l} - \Delta j_n^+ \sum_{k=0}^{N_{\rm tr}} c_{n+1,kA_n}\langle l|k\rangle_{A_{n+1}} \\ &-\Delta j_n^- \sum_{k=0}^{N_{\rm tr}} c_{n-1,kA_n}\langle l|k\rangle_{A_{n-1}} = E c_{n,l}, \end{aligned} \tag{6}$$

where the coefficients are ${}_{A_n}\langle l|k\rangle_{A_{n-1}} = (-1)^l D_{l,k}$ and ${}_{A_n}\langle l|k\rangle_{A_{n+1}} = (-1)^k D_{l,k}$, with

$$\begin{aligned} D_{l,k} &= e^{-G^2/2}\sum_{r=0}^{\min[l,k]} \frac{(-1)^{-r}\sqrt{l!k!}G^{l+k-2r}}{(l-r)!(k-r)!r!}, \\ G &= \frac{2\lambda}{\omega_0\sqrt{N}}. \end{aligned} \tag{7}$$

In the following work, we select the maximum truncation number $N_{\rm tr} = 50$, which is sufficient to give the convergent excited state energies with relative error less than 10^{-5}.

As is well known, in the thermodynamic limit $N \to \infty$ the Dicke model undergoes a transition from normal (ground state with zero photonic and atomic excitations) to superradiant (ground state with a macroscopic population) phase when the qubit-boson coupling strength crosses the critical value [99] $\lambda_c = \frac{1}{2}\sqrt{\omega_0\Delta\coth(\beta\omega_0/2)}$, with $\beta = 1/kT$ being the inverse of temperature. The zero and finite temperature transitions belong to different classes of universality with this difference manifested, for example, in photon-atom entanglement, which diverges for $T = 0$ and remains finite for $T \neq 0$. Moreover, when $N = 1$ the Dicke model is reduced to the seminal quantum Rabi model [66,67].

To help clarify the numerical results, we explore two limit regimes of our model: (i) the thermodynamic limit with $N \to \infty$ and $\sqrt{N}\lambda = \text{const}$ and (ii) the deep-strong coupling regime with fixed N and $\lambda \to \infty$. Both regimes allow one to derive a diagonalizable effective Hamiltonian through the Holstein-Primakoff (HP) representation of the angular

momentum operators, which maps the total spin operators $\hat{J}_\alpha$ to a bosonic mode $\hat{b}$.

To the case (i), the quantization axis is $\hat{J}_z$ and the HP transformation, $\hat{J}_z = (\hat{b}^\dagger\hat{b} - \frac{N}{2})$, $\hat{J}_+ = \hat{b}^\dagger\sqrt{N - \hat{b}^\dagger\hat{b}}$, $\hat{J}_- = \sqrt{N - \hat{b}^\dagger\hat{b}}\,\hat{b}$, leading to the large N limit ($N \gg \langle\hat{b}^\dagger\hat{b}\rangle$)

$$\hat{H}_{HP(N)} = \omega_0\hat{a}^\dagger\hat{a} + \Delta\hat{b}^\dagger\hat{b} + \lambda(\hat{a}^\dagger + \hat{a})(\hat{b}^\dagger + \hat{b}). \quad (8)$$

The above Hamiltonian can be diagonalized in the normal phase $\lambda \leqslant \sqrt{\omega_0\Delta}/2 = \lambda_c$ to $\hat{H}_{NP} = \varepsilon_-c_-^\dagger c_- + \varepsilon_+c_+^\dagger c_+$ with the energies given by

$$(\varepsilon_\pm)^2 = \frac{\omega_0^2+\Delta^2}{2} \pm \frac{1}{2}\sqrt{\left(\omega_0^2-\Delta^2\right)^2 + 16\lambda^2\omega_0\Delta}. \quad (9)$$

After a suitable displacement of the HP bosons, the superradiant phase $\lambda > \lambda_c$ can be cast in a bilinear form and diagonalized with the normal mode frequencies

$$(\varepsilon_\pm)^2 = \frac{\omega_0^2\lambda^4+\Delta^2\lambda_c^4}{2\lambda_c^4} \pm \frac{1}{2\lambda_c^4}\sqrt{\left(\omega_0^2\lambda^4-\Delta^2\lambda_c^4\right)^2 + 4\omega_0^2\Delta^2\lambda_c^8}. \quad (10)$$

The proper quantization axis to case (ii) is $\hat{J}_x$ and the HP leading Hamiltonian term to large $\lambda(N \gg \langle\hat{b}^\dagger\hat{b}\rangle)$ and eigenvalues' limit are

$$\hat{H}_{HP(\lambda)} = \omega_0\hat{a}^\dagger\hat{a} + \frac{4N\lambda^2}{\omega_0}\hat{b}^\dagger\hat{b} - N\lambda(\hat{a}^\dagger + \hat{a}),$$

$$E_{mn} = m\frac{4N\lambda^2}{\omega_0} + n\omega_0 - \frac{N^2\lambda^2}{\omega_0}. \quad (11)$$

We note that the eigenstates of $\hat{H}_{HP(\lambda)}$ are product states of photons' displaced Fock states and atomic states being x polarized. Furthermore, both limiting cases lead to decoupled quantum harmonic oscillators that can be used to calculate the average energy analytically for each stage of the thermodynamic cycle and hence the work and efficiency.

III. QUANTUM OTTO CYCLE

To perform a quantum Otto cycle, which is composed of two adiabatic and two isochoric processes [4,5], we consider N two-level atoms and one electromagnetic field mode, as described by the Dicke model, as the working substance. During the isochoric process we left the N atoms and the electromagnetic field to interact with a hot (cold) reservoir at temperature T_h (T_c). The four strokes of the quantum Otto cycle are described as follows (Fig. 1).

(1) Quantum isochoric process. The working substance as modeled by the Dicke Hamiltonian H_s^h with frequency $\omega = \omega_h$ is brought into contact with a hot reservoir at temperature T_h. In this process, the system undergoes a Markovian evolution, which is described by the quantum dressed master equation [92–96]

$$\frac{d}{dt}\hat{\rho}_s = -i[\hat{H}_0, \hat{\rho}_s] + \sum_{u;k<j}\left\{\Gamma_u^{jk}n_u(\Delta_{jk})\mathcal{D}[|\phi_j\rangle\langle\phi_k|, \hat{\rho}_s] + \Gamma_u^{jk}[1 + n_u(\Delta_{jk})]\mathcal{D}[|\phi_k\rangle\langle\phi_j|, \hat{\rho}_s]\right\}, \quad (12)$$

where $|\phi_k\rangle$ is the dressed eigenbasis of the Dicke Hamiltonian $\hat{H}$ as $\hat{H}_0|\phi_k\rangle = E_k|\phi_k\rangle$, $\mathcal{D}[\hat{O}, \hat{\rho}_s] = \frac{1}{2}[2\hat{O}\hat{\rho}_s\hat{O}^\dagger - \hat{\rho}_s\hat{O}^\dagger\hat{O} - \hat{O}^\dagger\hat{O}\hat{\rho}_s]$ is the dissipator, $\Gamma_u^{jk} = \gamma_u(\Delta_{jk})|S_u^{jk}|^2$ is the rate, with $S_q^{jk} = \frac{1}{\sqrt{N}}\langle\phi_j|(\hat{J}_+ + \hat{J}_-)|\phi_k\rangle$ and $S_c^{jk} = \langle\phi_j|(\hat{a}^\dagger + \hat{a})|\phi_k\rangle$, where we consider the Ohmic case $\gamma_u(\Delta_{jk}) = \pi\alpha(\Delta_{jk})\exp(-|\Delta_{jk}|/\omega_{co})$, with α being the coupling strength and ω_{co} being the cutoff frequency of the thermal baths. In the eigenbasis, the dynamics of the population $P_n = \langle\phi_n|\hat{\rho}_s|\phi_n\rangle$ is given by

$$\frac{d}{dt}P_n = \sum_{u,k\neq n}\Gamma_u^{nk}n_u(\Delta_{nk})P_k - \sum_{u,k\neq n}\Gamma_u^{nk}[1 + n_u(\Delta_{nk})]P_n, \quad (13)$$

where $\Gamma_u^{nk} = -\Gamma_u^{kn}$.

After a long enough evolution, the system will reach the only steady state $\rho_1 = \rho_{ss}(T_h) = \sum_n P_n^{ss}(T_h)|E_n^h\rangle\langle E_n^h|$ of Eq. (8) with $\frac{d\rho}{dt} = 0$, $P_n^{ss}(T_h)$ being the corresponding population. The system eigenstates $|\phi_k^h\rangle$ and eigenvalues E_k^h of H_s^h were obtained by using the extended bosonic coherent state approach method [75]. During this process, a heat amount Q_h is absorbed from the hot reservoir, without any work being done.

(2) Quantum adiabatic expansion process. The system is isolated from the hot reservoir and the energy levels are changed from E_n^h to E_n^c by varying the frequency from ω_h to ω_c (with $\omega_h > \omega_c$). This process must be done slow enough to ensure that the populations $P_n^{ss}(T_h)$ remain unchanged according to the quantum adiabatic theorem. At the end of this adiabatic expansion the state becomes $\rho_2 = \sum_n P_n^{ss}(T_h)|E_n^c\rangle\langle E_n^c|$. During this process only work is performed, with no heat being exchanged.

(3) Quantum isochoric process. The working substance with frequency $\omega = \omega_c$ and modeled by the Hamiltonian H_s^c is now put into contact with a cold reservoir at temperature $T_c < T_h$ until they reach thermal equilibrium. In this case, we have a change in the steady state population from $P_n^{ss}(T_h)$

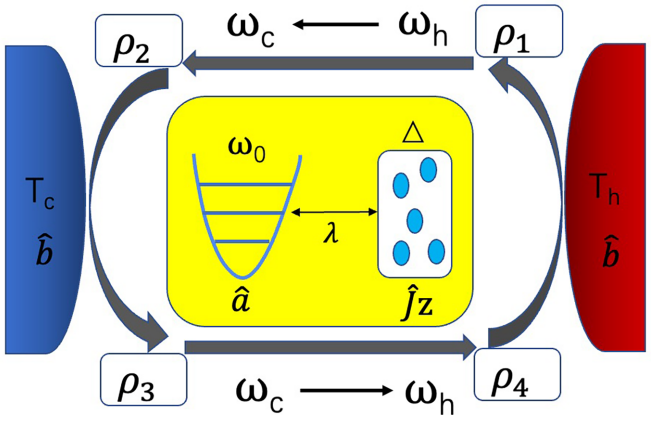

FIG. 1. Schematic representation of the four strokes of an Otto cycle for the realization of a universal heat machine based on the open Dicke mode, as detailed in Sec. III. During the isochoric stroke the frequency of the working substance, as modeled by the Dicke Hamiltonian, is held fixed while interacting with a hot (cold) reservoir at temperature T_h (T_c). Only heat is exchanged during this stroke. In the two quantum adiabatic strokes the working substance is isolated from the reservoir and has its frequency shifted, thus producing work. No heat is exchanged during this stroke. By controlling the parameters ω_0, Δ, and λ of the model the machine can work as an engine, refrigerator, heater, or accelerator.

to $P_n^{ss}(T_c)$, while the eigenvalues E_n^c of the system remain unchanged, and the state becomes $\rho_3 = \sum_n P_n^{ss}(T_c)|E_n^c\rangle\langle E_n^c|$. During this process, only heat is exchanged and an amount of heat Q_c is released to the reservoir, but no work is done.

(4) Quantum adiabatic compression process. The system is isolated from the cold reservoir and its energy levels are changed back from E_n^c to E_n^h by varying the frequency from ω_c to ω_h. At the end of the process, the populations P_n^{ss} (T_c) remain unchanged, the state becomes $\rho_4 = \sum_n P_n^{ss}(T_c)|E_n^h\rangle\langle E_n^h|$, and only work is performed on the working substance, but no heat is exchanged.

Next, let us calculate the work and heat exchanged in each stroke. According to the first law of thermodynamics, a quantum system with discrete energy levels can be written as

$$dU = \delta Q + \delta W = \sum_n \left(E_n dP_n^{ss} + P_n^{ss} dE_n\right), \tag{14}$$

where E_n are the energy levels and P_n^{ss} are the occupation probabilities at steady state. Accordingly, the heat Q_h (Q_c) exchanged with the hot (cold) reservoir and the net work W satisfy the following relations [20]:

$$Q_h = \sum_n E_n^h \left[P_n^{ss}(T_h) - P_n^{ss}(T_c)\right], \tag{15}$$

$$Q_c = \sum_n E_n^c \left[P_n^{ss}(T_c) - P_n^{ss}(T_h)\right], \tag{16}$$

$$W = Q_h + Q_c = \sum_n \left(E_n^h - E_n^c\right)\left[P_n^{ss}(T_h) - P_n^{ss}(T_c)\right]. \tag{17}$$

In this work we will adopt the following convention: $Q > 0$ $(Q < 0)$ correspond to absorption (release) of heat from (to) the reservoir, while $W > 0$ $(W < 0)$ correspond to work performed by (on) the quantum heat engine. There are only four working regimes allowed under not violating the Clausius inequality with the first law of thermodynamics [100]: (1) heat engine (E), $Q_h > 0$, $Q_c < 0$, and $W > 0$; (2) refrigerator (R), $Q_c > 0$, $Q_h < 0$, and $W < 0$; (3) heater (H), $Q_c < 0$, $Q_h < 0$, and $W < 0$; (4) accelerator (A), $Q_c < 0$, $Q_h > 0$, and $W < 0$. In this article we are more concerned with the heat engine and the refrigerator, which are of most interest for useful applications and whose figures of merit are the efficiency $\eta = \frac{W}{Q_h}$ and the coefficient of performance (COP) $\xi = \frac{Q_c}{|W|}$, respectively.

IV. RESULTS AND DISCUSSIONS

A. Working regimes for the universal quantum Otto machine based on the ODM

We can gain some insight into the Otto cycle by making a qualitative description of the different working regimes for the universal QOHM, as shown in Fig. 2 for $N = 8$ two-level atoms and $\omega_h/\omega_c = 2$. Note that given two operating temperatures of the Otto cycle, by controlling the parameter λ we obtain the four different types of machine. Also, note that the four regions are all present at low temperatures, Figs. 2(a)–2(c), and mainly occupied by refrigerator (cyan area) and heat engine (magenta area). As the temperature rises, Figs. 2(d), the engine and refrigerator operating regions stand out even more. Figures 2(a)–2(c) show that heat engine and refrigerator regions are mainly distributed in weak coupling and

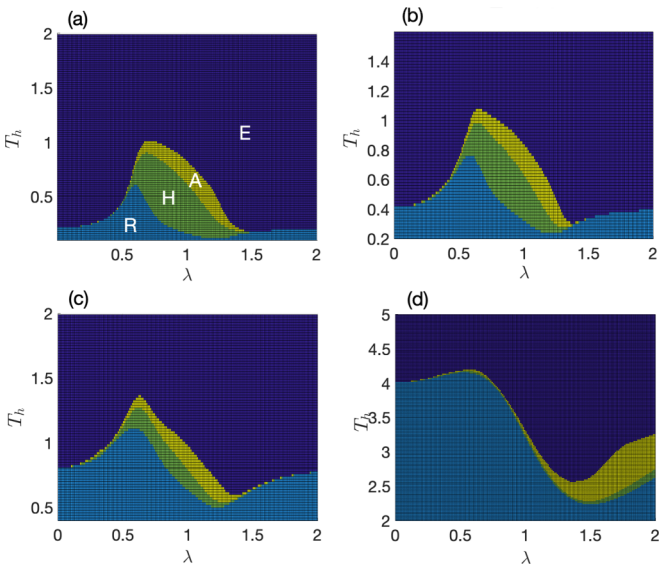

FIG. 2. (a)–(d) Various operating regimes of the quantum Otto machine achieved by varying the temperatures of the hot thermal reservoir T_h and the qubit-boson coupling strength λ, both in units of ω, keeping fixed the temperature of the cold thermal reservoir, also in units of ω as (a) $T_c = 0.1$, (b) $T_c = 0.2$, (c) $T_c = 0.4$, and (d) $T_c = 2$. The color code stands for heat engine (magenta), refrigerator (cyan), heater (green), and accelerator (yellow). The other system parameters are given by $N = 8$, $\omega_h = 2\omega$, and $\omega_c = \omega$.

ultrastrong regimes. Strikingly, up to $\lambda \approx 0.3$ and for $\lambda \gg 2$, due to the relative harmonicity of the spectrum, the positive-work condition (PWC) follows the one for the quantum harmonic oscillator or qubit, i.e., $T_h > \frac{\omega_h}{\omega_c} T_c$.

Next, we analyze the work regimes for the universal QOHM for different numbers N of qubits when the temperatures of the hot and cold thermal reservoirs are fixed. Figure 3 shows the (a) work W, (b) heat Q_h, and (c) heat Q_c as a function of the qubit-boson coupling strength λ for different values of the qubits' number N, thus evidencing the four working regimes for different qubits' numbers. As mentioned above, the heat engine is distributed in the weak and strong coupling regimes and the deep strong coupling regime, whereas the PWC $T_h > \frac{\omega_h}{\omega_c} T_c$ is satisfied, while the refrigerator, heater, and accelerator are located around the critical coupling $\lambda_c = \frac{1}{2}\sqrt{\omega_0 \Delta \coth(\beta\omega_0/2)}$, where the spectrum is highly anharmonic. Note that increasing the number of N qubits shifts the engine region to the left, allowing engines to be built for smaller values of λ as N grows. On the right side, in the deep strong regime, this behavior is maintained: as N grows, the region corresponding to the engine also shifts to the left, increasing the area corresponding to the engine. It is to be noted that for $\lambda \lesssim 0.4$ and for $\lambda \gtrsim 1.5$ the work extracted by the engine practically remains constant with the increase of N. This behavior is mimicked by the amounts of heat Q_h and Q_c exchanged with the reservoirs. Given that increasing the number of atoms means that more work and heat can be exchanged, it is somewhat surprising that for certain values of λ increasing N these quantities remain unchanged. On the other hand, for the other types of machines, whose regions correspond to the middle region of Fig. 3, the exchanged work and heat increases with N.

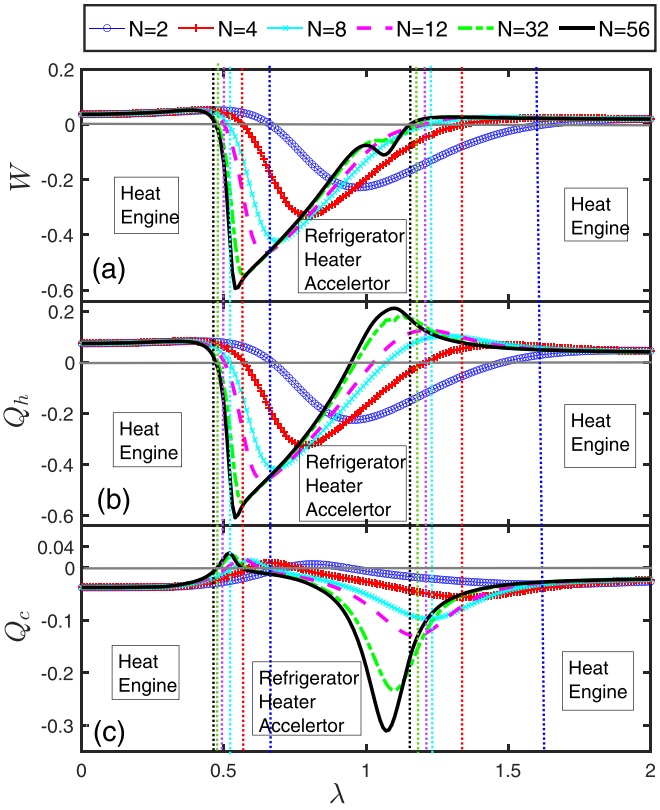

FIG. 3. (a) Work output W, (b) heat Q_h, and (c) heat Q_c as a function of the qubit-boson coupling strength λ for different number of qubits $N = 2$ (solid blue line with circles), $N = 4$ (solid red line with plus sign), $N = 8$ (solid cyan line with cross sign), $N = 12$ (dished magenta line), $N = 32$ (dash dot green line), and $N = 56$ (solid black line). Vertical dotted lines divide the different operating regimes of our universal quantum Otto heat machine by the same color used to designate the number N of atoms. The solid horizontal gray line indicates the zero of each quantity. The other system parameters are given by $T_h = 0.5$, $T_c = 0.1$, $\omega_h = 2\omega$, and $\omega_c = \omega$. All quantities above are in units of ω.

B. Efficiency and coefficient of performance

Next, we study the efficiency and COP of the Otto quantum engine and the refrigerator, which are the heat machines of greatest practical interest. To help our analysis, it is useful to recall the analytical result of efficiency $\eta_{\lambda=0} = 1 - \omega_c/\omega_h$, and COP $\xi_{\lambda=0} = \omega_c/(\omega_h - \omega_c)$, of an Otto cycle when $\lambda = 0$, which corresponds to N qubits and a noninteracting bosonic mode. First, we focus on the engine. In Figs. 4(a), 4(b), and 4(c) we plot efficiency as a function of the qubit-boson coupling strength λ for different number of qubits $N = 2$ (solid blue line with circles), $N = 4$ (solid red line with plus sign), $N = 8$ (solid cyan line with cross sign), $N = 12$ (dished magenta), $N = 32$ (dash dot green), $N = 56$ (dashed dark blue), and the thermodynamic limit $N \to \infty$ (solid black) with fixed $T_h = 0.5$, $T_c = 0.1$ for Figs. 4(a) and 4(b) and $T_h = 6$, $T_c = 2$ for Fig. 4(c). Figures 4(d) and 4(e) with $T_c = 0.1$, and Fig. 4(f) with $T_c = 2$, show the efficiency for various temperature ratios when varying the qubit-boson coupling strength λ with fixed $N = 8$. The drop to zero in efficiency, Figs. 4(a) and 4(d), and its growth from zero to a maximum, Figs. 4(b) and 4(e), occur due to the transition from the engine to the refrigerator regime, corresponding to the regions shown in Fig. 3. But, in any case, it is notable that the falls to zero and the rises to the maximum occur suddenly rather than smoothly. In particular, for $\lambda \lesssim 0.3$ the efficiency is independent of the number of atoms used as a working substance. Also, note that the efficiency drops to zero for smaller values of λ as N grows, as shown in Figs. 4(a) and 4(d), because of the shift of the engine region to the left as N grows, as already mentioned when analyzing Fig. 3.

The main advantage of the ODM over the decoupled system as a working substance happens around the critical region $\lambda_c = \frac{1}{2}\sqrt{\omega_0 \Delta \coth(\beta\omega_0/2)}$, where $\eta > \eta_{\lambda=0}$ only to $\lambda < \lambda_c$, an unexpected result, which means the normal phase of the Dicke model is more suitable to the engine operation than the superradiant phase, as depicted in Figs. 4(a)–4(f). Remarkably, for small temperatures as in Fig. 4(a) the number of qubits saturates quickly to the thermodynamic limit $N \to \infty$, with $N \approx 30$ being enough to extract the maximum efficiency.

Note that all the calculations we performed were done assuming thermal equilibrium. Driven-dissipative open Dicke models are being intensively studied in the context of nonequilibrium phase transitions [99] and, although relevant to the case where the four-stroke quantum Otto cycle is carried out in finite time, where the state of the system is not thermal, it is beyond the scope of this work and has not been considered.

Interestingly, for values of temperature ratios for which there is always the engine condition, see Figs. 4(c) and 4(f) and also Fig. 2, there is still a drop below the $\eta_{\lambda=0}$ around the critical coupling. In the deep-strong coupling regime, the efficiency tends to $\eta = 0.5$, which is predicted by the effective Hamiltonian Eq. (11) and the harmonicity of the spectrum for the considered temperatures. We point out that, to small number of atoms $N = 8$, there is a decrease in the engine operating region as the temperature gap increases as shown in Fig. 4(d), with the smallest region corresponding to $T_c/T_h = 1/3$ (solid black line). Second, note that the efficiency is smaller the greater the temperature gap is—a somewhat expected behavior when compared with the Carnot efficiency $\eta_{\text{Carnot}} = 1 - T_c/T_h$. As expected, the efficiency of our universal QOHM based on the open Dicke model never exceeds the Carnot efficiency. From Figs. 4(a), 4(b), 4(d), and 4(e), it would appear that the abrupt drop and sudden resurgence of efficiency values is a characteristic of engine efficiency. However, as can be seen from Figs. 2(a)–2(d), which shows the region of the various machines, there are temperature ratios for which there will always be a condition for the engine to exist. For these temperature ratios, there will be neither a sudden decrease to zero nor, consequently, an abrupt resurgence in efficiency. In fact, for $T_c > 1.0$ in Fig. 2(a), $T_c > 1.2$ in Fig. 2(b), $T_c > 1.5$ in Fig. 2(c), and $T_c > 4.5$ in Fig. 2(d) the engine condition will always be fulfilled. This behavior is exemplified in Figs. 4(c) and 4(f), where we explored other temperature ratios for fixed $N = 8$ and $T_c = 2$. Note from Fig. 4(c) that, in addition to the abrupt drop in efficiency, which is a signature of the passage from the region that determines engine condition to that of refrigerator, for $N = 2$, 4, and 8, there is also a smooth drop and rise, indicating that despite the increase of λ the engine condition continues to be satisfied.

Next, we focus on the refrigerator regime. In Fig. 5 the COP ξ as a function of the qubit-boson coupling strength is

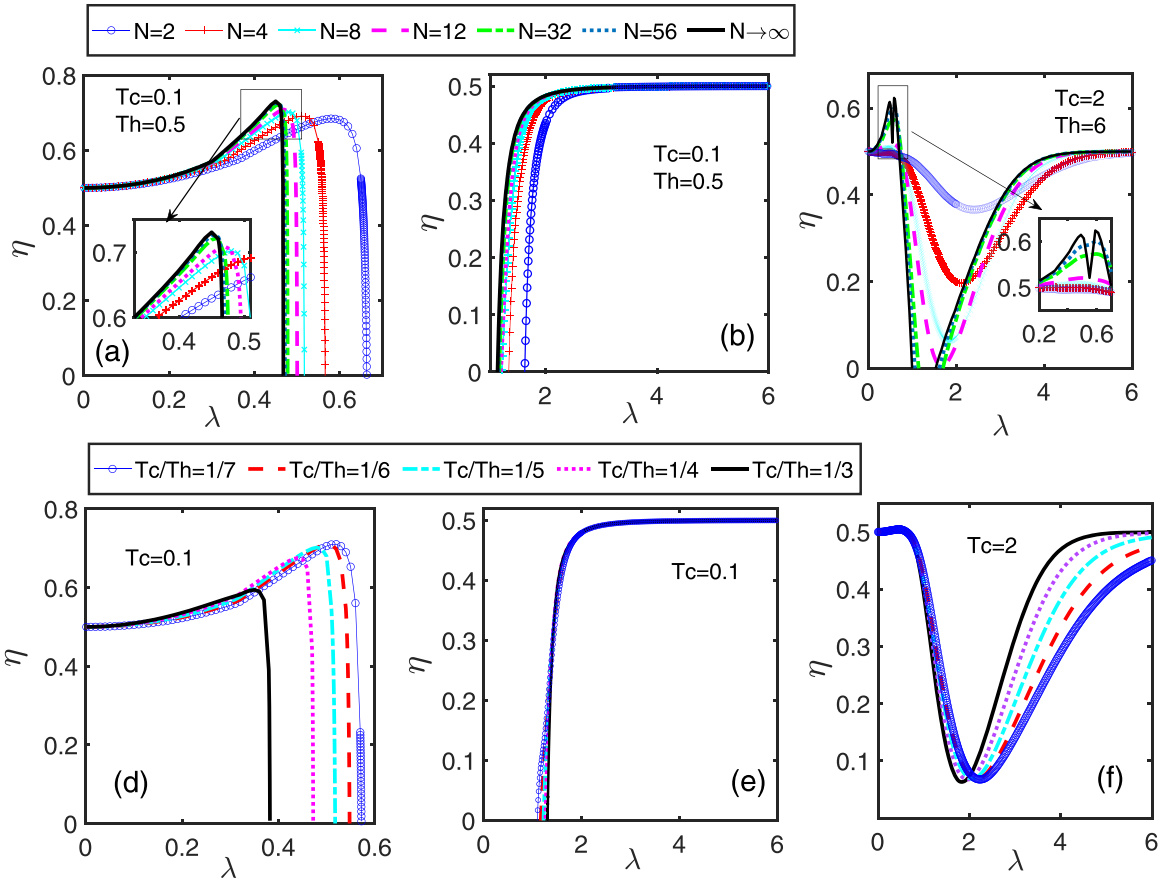

FIG. 4. Efficiency η of the quantum heat engine as a function of the qubit-boson coupling strength λ (in units of ω) for different number of qubits $N = 2$ (solid blue line with circles), $N = 4$ (solid red line with plus sign), $N = 8$ (solid cyan line with cross sign), $N = 12$ (dashed magenta line), $N = 32$ (dash dot green line), $N = 56$ (dotted deep blue line), and infinity N (solid black line), with fixed $T_h = 0.5$, $T_c = 0.1$ for (a), (b) and $T_h = 6$, $T_c = 2$ for (c). Likewise, (d) and (e) and (f) are for the efficiency η of the quantum heat engine as a function of the qubit-boson coupling strength λ under different temperature ratios $T_c/T_h = 1/7$ (solid blue line with circles), $T_c/T_h = 1/6$ (dashed red line), $T_c/T_h = 1/5$ (dash dot cyan line), $T_c/T_h = 1/4$ (dotted magenta line), $T_c/T_h = 1/3$ (solid black line), and fixed $N = 8$, with cold reservoir temperatures $T_c = 0.1$ for (d), (e) and $T_c = 2$ for (f). Here the temperatures are in units ω. The other system parameters are given by $\omega_h = 2\omega$, $\omega_c = \omega$.

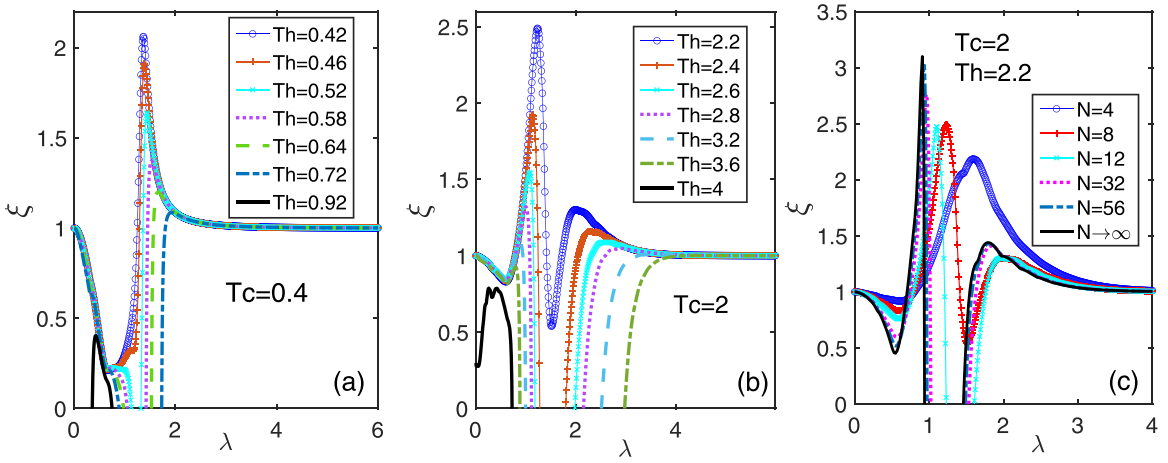

FIG. 5. Panels (a) and (b) show the COP ξ as a function of the qubit-boson coupling strength λ (in units of ω) for different T_h with fixed (a) $T_c = 0.4$, (b) $T_c = 2$, and $N = 8$ qubits. (c) COP ξ as a function of the qubit-boson coupling strength λ (in units of ω) under different qubit numbers with fixed $T_c = 2$, $T_h = 2.2$. The temperatures are in units of ω. The other parameters of the system are $\omega_h = 2\omega$, $\omega_c = \omega$.

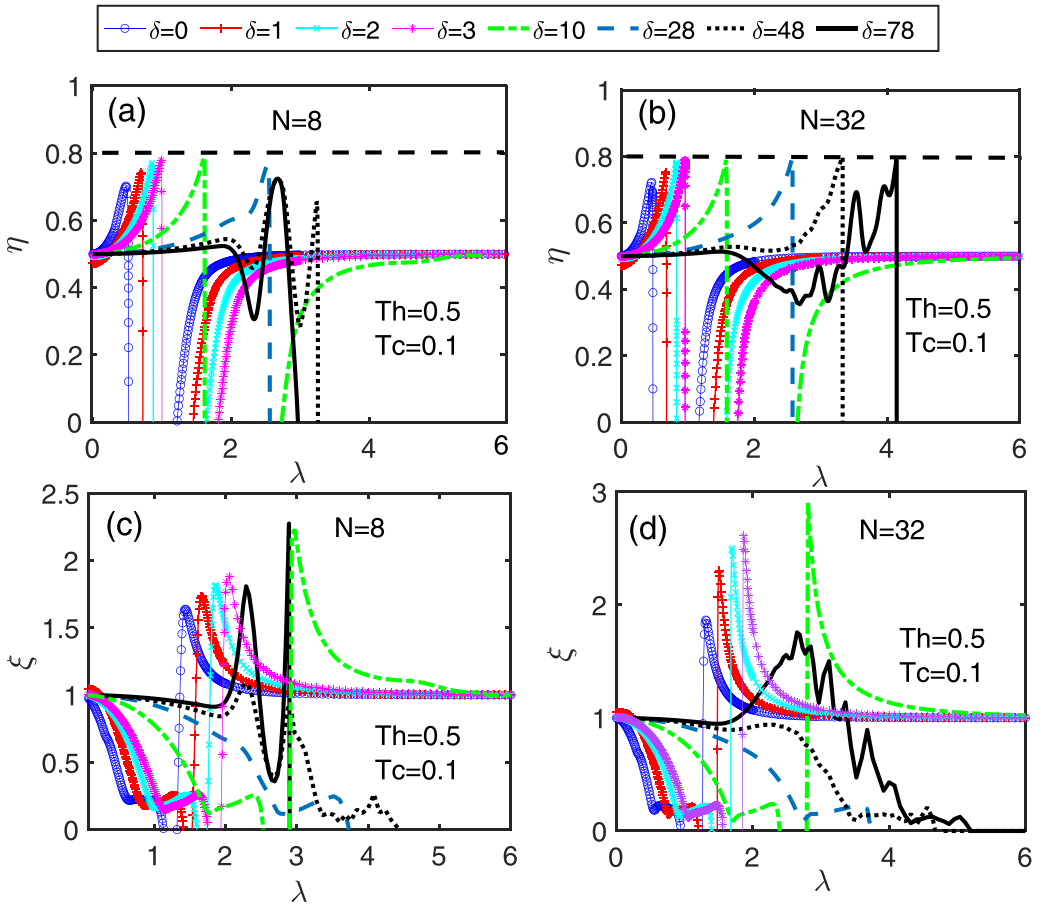

FIG. 6. (a),(b) Efficiency η (c),(d) and COP ξ as a function of the detuning $\delta = \omega - \Delta$ between the frequency ω of the field mode in the cavity and the frequency Δ of each of the N atoms. For comparison, the resonance case $\delta = 0$ is shown in the solid (blue) curve. The temperatures are fixed at $T_c = 0.1$ and $T_h = 0.5$, while the number of atoms is $N = 8$ in (a),(c) and $N = 32$ in (b),(d). The dashed horizontal line in (a),(b) indicates the Carnot limit for the efficiency of a thermal engine. These figures are symmetric for negative detuning δ.

investigated for several ratios of temperatures with fixed $N = 8$ and $T_c = 0.4$, Fig. 5(a), and $T_c = 2$, Fig. 5(b). In Fig. 5(c) we see the effect of the number of qubits on the COP ξ. It is noteworthy that, for the normal phase, for all temperatures and number of qubits, we found $\xi < \xi_{\lambda=0}$. Besides, similar to the heat engine in the deep-strong coupling regime, the effective Hamiltonian Eq. (11) leads to an accurate result of $\xi = \xi_{\lambda=0}$. As evidenced from Figs. 5(a)–5(c), the region of coupling $\lambda_c < \lambda \leqslant 3$ is where the COP for universal QOHM having the Dicke model as a working substance surpass that of the decoupled system used to fuel the quantum refrigerator. In addition, as observed in Figs. 5(a) and 5(b), the COP strongly depends on the temperature ratio, thus differing from $\xi_{\lambda=0} = \omega_c/(\omega_h - \omega_c)$, being higher to small temperature ratios, as the Carnot COP, keeping the limit $\xi \ll \xi_{\text{Carnot}} = T_c/T_h - T_c$. We note from Fig. 5 that for ratios of temperature where the universal QOHM would work as heat engine with $\lambda = 0$ (uncoupled case), corresponding to $\frac{T_h}{T_c} < \frac{\omega_h}{\omega_c}$, for some coupling ranges the universal QOHM works as a refrigerator with COP lower than that of the uncoupled case.

So far we have only considered the case of resonant interaction; now we will investigate how detuning $\delta = \Delta - \omega$ between the frequency Δ of each of the N qubits and the frequency ω of the field mode in the cavity affects the UQHM figures of merit. Figure 6 shows the efficiency (a),(b) and COP (c),(d) for several values of δ. The resonance case, $\delta = 0$, is shown in the solid (blue) with circles curve; the other curves are for the nonresonance cases. The efficiency, Fig. 6(a) for $N = 8$ and Fig. 6(b) for $N = 32$, presents several peaks, with its maximum value demarcated by the Carnot limit indicated by the horizontal dashed curve. Notice how, for certain values of the coupling parameter λ, the efficiency initially increases until it is very close to the maximum for $N = 8$ or always reaches its maximum value for $N = 32$. Note also that, as the detuning δ increases, the peaks corresponding to the maximum efficiency values shift to the right, that is, towards larger values of the coupling parameter λ. Similarly, the behavior of COP, Figs. 6(c) and 6(d), also presents maximum peaks, which also occur for higher values of λ as the detuning δ increases. Unlike efficiency, however, note how COP initially decreases before starting to increase until reaching the maximum, which only occurs for coupling values $\lambda > 1$. These results indicate that detuning is an important control parameter to be optimized to obtain the best thermal performance for both efficiency and the COP and must be taken into account when considering finite time process.

Lastly, we explore in Figs. 7(a)–7(c) the effect of the frequency ratio ω_h/ω_c on the work exchanged, Fig. 7(a), as well

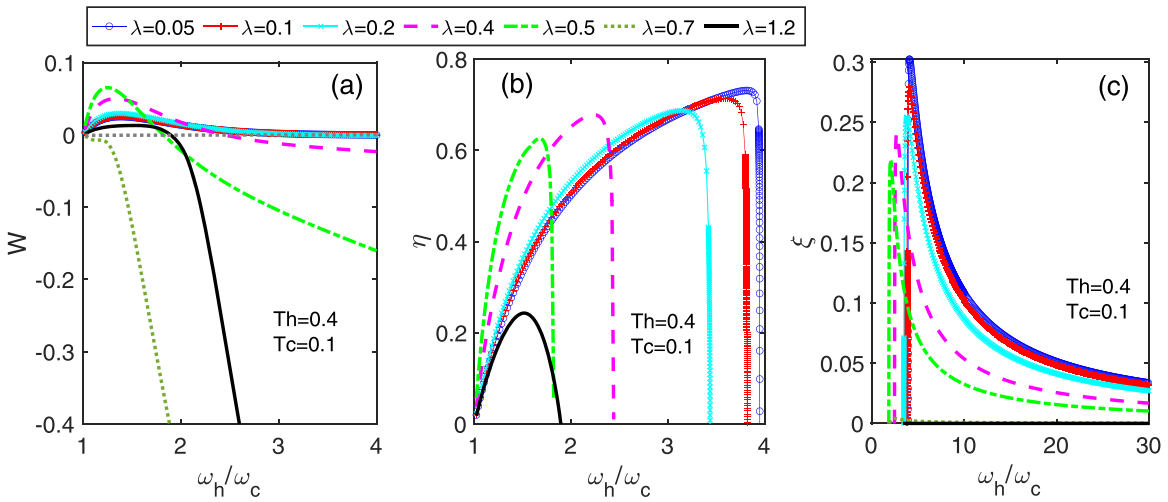

FIG. 7. (a) Work W, (b) efficiency η, and (c) COP as a function of the frequency ratio ω_h/ω_c for coupling strength $\lambda = 0.05$ (solid blue line with circles), $\lambda = 0.1$ (solid red line with plus sign), $\lambda = 0.2$ (solid cyan line with cross sign), $\lambda = 0.4$ (dashed magenta line), $\lambda = 0.5$ (dash dot green line), $\lambda = 0.7$ (dash dot deep green line), and $\lambda = 1.2$ (solid black line). The temperatures of the cold and hot reservoirs, given in units of ω, were fixed at $T_c = 0.1$ and $T_h = 0.4$, respectively. The number of qubits is fixed to $N = 8$.

as on the efficiency, Fig. 7(b), and performance, Fig. 7(c), for the universal QOHM. The coupling strengths are $\lambda = 0.05$ (solid blue line with circles), $\lambda = 0.1$ (solid red line with plus sign), $\lambda = 0.2$ (solid cyan line with cross sign), $\lambda = 0.4$ (dashed magenta line), $\lambda = 0.5$ (dash dot green line), $\lambda = 0.7$ (dash dot deep green line), and $\lambda = 1.2$ (solid black line). The temperatures were fixed as $T_c = 0.1$ to the cold thermal reservoir and $T_h = 0.4$ to the hot thermal reservoir. The frequency ratios, in addition to indicating more clearly the PWC condition, also allow for extracting the point that maximizes both the efficiency and the COP for the universal QOHM. Note the same behavior already observed in other figures, both for efficiency and for COP. In Fig. 7(b) we see that after a growth until reaching a maximum, there is an abrupt drop, precisely at the point where the engine operating condition changes to the refrigerator condition. In Fig. 7(c), where there is a sudden appearance of COP in the refrigerator region, the COP also reaches a maximum and then decreases smoothly. The value of the maximum frequency ratio can thus be used to maximize both efficiency and COP, and for the engine this condition is the so-called efficiency at maximum power [23].

To finish this section, we point out that we also studied two other protocols to carry out the adiabatic processes, namely (i) keeping the frequencies constant and changing the coupling strength and (ii) changing the number of qubits that interact with the quantum mode and fixing both the frequencies and the coupling strength. As verified by our numerical calculations (not shown here), in both protocols the efficiency and the coefficient of performance do not overcome the case in which the working substance is composed of a field mode decoupled from the qubits.

C. Quantum correlations at thermal equilibrium

In this section, we investigate whether quantum correlations are present at thermal equilibrium and, if so, whether they affect the efficiency or COP of the universal quantum heat machine (UQHM) based on the open Dicke model (ODM). In accordance with our analytical and numerical studies, shown in Figs. 8(a)–8(f), we claim that quantum properties surviving thermalization are not the reason for the superior performance of efficiency, extractable work, and COP for the UQHM based on the ODM. The improvements we observed both in efficiency (Fig. 5) and COP (Fig. 6) are due to the structure of the energy levels, as evidenced by the validity condition $N \gg \langle \hat{b}^\dagger \hat{b} \rangle$ to derive the effective Hamiltonian Eq. (8), that is, small temperatures require a smaller number of qubits to lead to the anharmonicity around the critical point that is present at all temperatures in the thermodynamic limit.

To calculate quantum correlations, we resort to the following complementary quantities: (i) the second-order correlation function, which captures the occurrence of sub-Poissonian statistics to the electromagnetic field inside the cavity, (ii) the negativity, which quantifies atom-field entanglement, and (iii) the spin quadrature, which quantifies the degree of squeezing for the atomic variables and is a witness of quantum entanglement between the two level systems. We emphasize that other quantum measures, such as mutual information, photon squeezing, and quantum discord, were investigated and omitted because they showed the same general behavior of the considered quantities.

First, note that the conventional definition of the normalized zero-delay second-order correlation function is [101]

$$g^{(2)}(0) = \frac{\langle (\hat{a}^\dagger)^2 (\hat{a})^2 \rangle}{\langle \hat{a}^\dagger \hat{a} \rangle^2}. \tag{18}$$

This quantity describes the probability of detecting two photons simultaneously. This definition holds for weak light-matter couplings, where the intracavity photons, whose annihilation operator is described by $\hat{a}$, suffice to explain the observed photon correlations. On the other hand, in the USC regime, where the qubit system strongly dresses the bosonic field, the second-order correlation function is derived from the

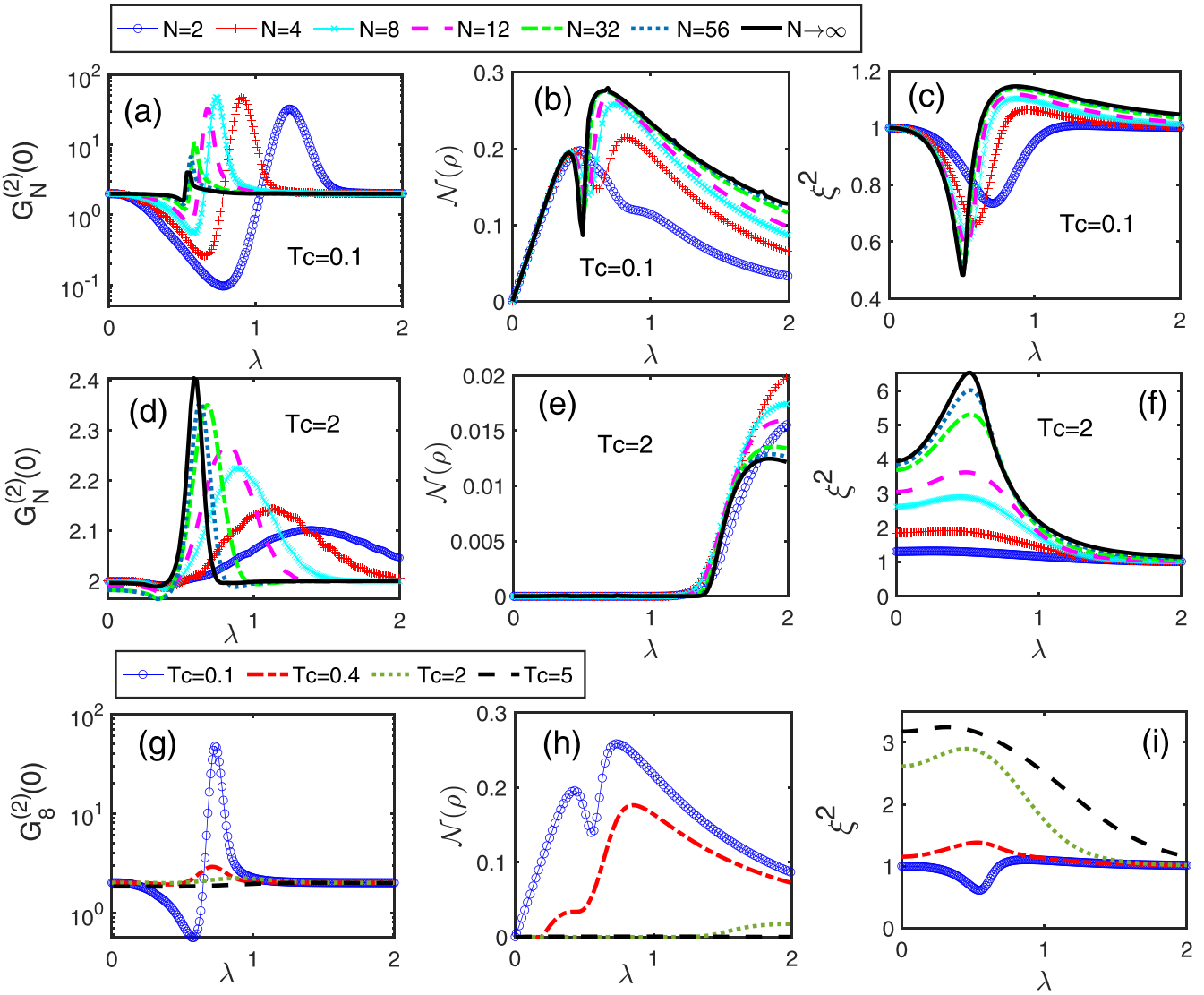

FIG. 8. Two-photon correlation function $G_N^{(2)}(0)$ (a),(c),(e) and negativity $\mathcal{N}(\rho)$ (b),(d),(f) as a function of the coupling strength λ. In (a)–(c) the two-photon correlation function, negativity, and the spin quadrature parameter are shown for several qubit number N, including the thermodynamic limit, with the cold thermal reservoir temperature fixed at $T_c = 0.1$ (a)–(c) and $T_c = 2$ (d)–(f). In (g)–(i), the qubit number was fixed at $N = 8$ and the cold thermal reservoir temperature was chosen as $T_c = 0.1$ (solid blue line with circles), $T_c = 0.4$ (red dash line), $T_c = 0.2$ (green dot line), and $T_c = 5$ (black dash line). The other system parameters are $\omega_c = \omega$. The coupling strength λ and temperatures are in units of ω.

input-output formalism as [102,103]

$$G^{(2)}(0) = \frac{\langle(\hat{X}^-)^2(\hat{X}^+)^2\rangle}{\langle\hat{X}^-\hat{X}^+\rangle^2}, \tag{19}$$

where

$$\hat{X}^+ = -i\sum_{k>j}\Delta_{kj}X_{jk}|\phi_j\rangle\langle\phi_k|, \tag{20}$$

with $\hat{X}^- = (\hat{X}^+)^\dagger$, $\Delta_{kj} = E_k - E_j$ is the energy gap, and $X_{jk} = \langle\phi_j|(\hat{a}^\dagger + \hat{a})|\phi_k\rangle$. Here, X_{jk} describes the transition from the higher eigenstate $|\phi_k\rangle$ to the lower one $|\phi_j\rangle$. Notice that, in the weak qubit-photon interaction limit (i.e., $\lambda_i \ll 1$), the operator $\hat{X}^+$ is reduced to $\hat{X}^+ = -i\omega\hat{a}$. Thus the correlation function in Eq. (19) simplifies to the conventional case. When $G^{(2)}(0) < 1$ the light presents the nonclassical effect of antibunching and can be taken as an unequivocal indication of quantumness.

As for the negativity $\mathcal{N}(\rho)$ of a subsystem A, it can be defined in terms of a density matrix ρ as [104,105]

$$\mathcal{N}(\rho) = \frac{\|\rho^{T_A}\|_1 - 1}{2}, \tag{21}$$

where ρ^{T_A} is the partial transpose of ρ with respect to subsystem A and $\|X\|_1 = \mathrm{Tr}|X| = \mathrm{Tr}\sqrt{X^\dagger X}$ is the trace norm or the sum of the singular value for the operator X. Nonzero negativity values indicate the presence of quantum correlations in the form of entanglement, being greater the greater the amount of entanglement present.

To study atomic correlations we use the spin squeezing parameter, which also is a measure of entanglement between

atoms. According to Kitagawa and Ueda, the spin squeezing parameter is defined as [106]

$$\xi^2 = \frac{2(\Delta S_{\vec{n}_\perp})^2}{J} = \frac{4(\Delta S_{\vec{n}_\perp})^2}{N}, \tag{22}$$

where $\vec{n}_\perp$ refers to an axis perpendicular to the mean spin $\langle \vec{S} \rangle$ and $S_{\vec{n}_\perp} = \vec{S} \cdot \vec{n}_\perp$. Spin squeezing parameter $\xi^2 < 1$ indicates that the system is spin squeezed.

We computed $G^{(2)}(0)$ in Figs. 8(a), 8(d), and 8(g), $\mathcal{N}(\rho)$ in Figs. 8(b), 8(e), and 8(h), and the spin parameter ξ^2 in Figs. 8(c), 8(f), and 8(i) as a function of the coupling strength λ for different numbers of qubits. In Figs. 8(g), 8(h), and 8(i) we set $N = 8$ and investigated the effect of different temperatures on the quantumness of the work substance. Note that the quantum correlations are degraded by increasing the number N of qubits and increasing the temperature T_h, whereas η and ξ increase with the number of qubits for all temperatures. If we compare Figs. 8(a)–8(i) showing maximum antibunching, maximum entanglement, and spin squeezing with Figs. 4(a)–4(f) and 5(a), 5(b) which respectively show efficiency and COP, we will see that there is no correspondence between the maximum of quantum correlations and the maximum of efficiency and COP.

As far as the second-order correlation is concerned, the efficiency is higher in the deep strong coupling regime ($\lambda > 2$), Figs. 4(b) and 4(e), and, therefore, far from the region where the second-order correlation shows the sub-Poissonian effect. The same conclusion can be drawn from Figs. 5(a)–5(c) for the COP, whose maxima lie in regions far from the value of the critical parameter λ. With regard to negativity, Figs. 7(b), 7(e), and 7(h) show that the maximum of negativity, and therefore of entanglement, does not coincide with the maximum of efficiency and COP. For example, in Fig. 4(b) for $T_c = 0.1$ and various values of N, the efficiency is practically constant with the coupling parameter and therefore independent of the amount of entanglement, whereas in Fig. 7(b) the negativity, also at $T_c = 0.1$, and the various values of N present maximums and minimums when varying the coupling parameter. The same can be said about the COP: there is nothing in the analysis of the maximums that indicates the relevance of negativity for its improvement. Take, for example, Fig. 7(d) for $T_c = 2$, where negativity remains zero for a large range of values of λ and then increases monotonically until to $\lambda = 2$, with similar behavior even for different values of N. Compare with Fig. 5(c), where the COP has a very different behavior depending on N, with no correspondence with negativity.

Consider now the spin quadrature parameter, where Fig. 7(c) indicates the presence of squeezing and entanglement with maxima close to the critical point at $T_c = 0.1$ and for all values of N. When we look at the efficiency and the COP, Figs. 4 and 5, respectively, we see that there is no correspondence between the atomic squeezing and the UQOHM figures of merit. Also, while at $T_c = 2$ Fig. 7(c) shows that there is no squeezing for all N, Fig. 4(f) shows that the efficiency passes through a maximum before decreasing. These same conclusions are supported by additional numerical calculations that we performed (not shown here). To summarize this section, and as previously mentioned, we point out that the improvement in the efficiency and performance of the UQOHM using the Dicke model as the working substance cannot be attributed to quantum resources [107,108], but it is due to the high anharmonicity of the spectrum around the critical point of the Dicke model.

Our UQOHM protocol presents nontrivial experimental challenges, mainly involving coupling strength and low-temperature environments. Although the physical model considered is general and has been implemented in a large number of systems [109–111], standard ways of generating the Dicke model in the laboratory involve driven dissipative systems that give rise to a nonequilibrium scenario. We anticipate that our proposal may be susceptible to experimental implementation through extensions of current implementations of the USC and DSC realizations of the Rabi model [83–91], for the case of N qubits with incoherent collective processes leading to an equilibrium thermal steady state.

V. CONCLUSION

In summary, in this work we propose a universal quantum Otto heat machine (UQOHM) based on the open Dicke model (ODM). The ODM is composed of N atoms of two levels (qubits) that interact with a mode of the electromagnetic field and both the mode and the N qubits, which constitute the working substance of the universal machine, interact with thermal reservoirs. This model presents a critical point and can be solved analytically in the thermodynamic limit $N \to \infty$. By universal thermal machine we mean that it is possible, by adjusting the atom-field coupling parameter λ of the ODM, to build all types of thermal machines, namely engines, refrigerators, heaters, and accelerators. Focusing on engines and refrigerators, which are the machines with the greatest applicability, we show, for a wide temperature range and a large number of qubits, including in the thermodynamic limit, how the engine efficiency and the performance coefficient of the refrigerator change with the parameter λ of the ODM.

We also conducted a study of the quantum correlations present in the ODM using the second-order correlation function, negativity, and spin squeezing, showing that, for certain values of the coupling parameter λ of the Dicke model, both the antibunching effect and the entanglement survive thermalization. Next, we show that it is possible, close to the critical point, to obtain both an efficiency and a performance for the UQOHM that is greater than the case in which the system is uncoupled, thus showing the advantage of using the Dicke model as the working substance. Furthermore, the detailed study of the second-order correlation function, negativity, and atomic spin quadrature indicates that there is no correspondence between the improvement in efficiency and COP of the UQOHM and the quantum resources arising from antibunching, spin quadrature, and entanglement. This claim is strongly supported by the disappearance of all quantum quantifiers adopted at moderate temperatures where, by increasing the number of atoms, it is still possible to surpass the efficiency and COP of a system that uses uncoupled atoms and field as working fluid. This effect is absent in previous studies using the Rabi model which, unlike what we found here, led to associating gains in efficiency and COP with the presence of quantum correlations.

Addressing intriguing questions for further investigation in the context of finite-time thermodynamics involves exploring the fluctuations and statistical distribution of work and heat [112–114] and, additionally, gaining insight into the influence of criticality in the working substance, as presented in the Dicke model, within the bounds of nonequilibrium fluctuations of many-body quantum thermal engines [115].

ACKNOWLEDGMENTS

We acknowledge financial support from the Brazilian agencies CNPq and FAPEG. This work was performed as part of the Brazilian National Institute of Science and Technology (INCT) for Quantum Information Grant No. 465469/2014-0. H.-G.X. and J.J. are supported by the National Natural Science Foundation of China under Grant No. 11975064.

[1] H. E. D. Scovil and E. O. Schulz-DuBois, Three-level masers as heat engines, Phys. Rev. Lett. **2**, 262 (1959).
[2] R. Alicki, The quantum open system as a model of the heat engine, J. Phys. A: Math. Gen. **12**, L103 (1979).
[3] R. Kosloff, A quantum mechanical open system as a model of a heat engine, J. Chem. Phys. **80**, 1625 (1984).
[4] H.-T. Quan, Y.-X. Liu, C.-P. Sun, and F. Nori, Quantum thermodynamic cycles and quantum heat engines, Phys. Rev. E **76**, 031105 (2007).
[5] H. T. Quan, Quantum thermodynamic cycles and quantum heat engines. II, Phys. Rev. E **79**, 041129 (2009).
[6] N. Brunner, N. Linden, S. Popescu, and P. Skrzypczyk, Virtual qubits, virtual temperatures, and the foundations of thermodynamics, Phys. Rev. E **85**, 051117 (2012).
[7] R. Kosloff, Quantum thermodynamics: A dynamical viewpoint, Entropy **15**, 2100 (2013).
[8] R. Kosloff and A. Levy, Quantum heat engines and refrigerators: Continuous devices, Annu. Rev. Phys. Chem. **65**, 365 (2014).
[9] J. Goold, M. Huber, A. Riera, L. D. Rio, and P. Skrzypczyk, The role of quantum information in thermodynamics—A topical review, J. Phys. A **49**, 143001 (2016).
[10] S. Vinjanampathy and J. Anders, Quantum thermodynamics, Contemp. Phys. **57**, 545 (2016).
[11] J. Millen and A. Xuereb, Perspective on quantum thermodynamics, New J. Phys. **18**, 011002 (2016).
[12] R. Kosloff and Y. Rezek, The quantum harmonic Otto cycle, Entropy **19**, 136 (2017).
[13] S. Deffner and S. Campbell, *Quantum Thermodynamics: An Introduction to the Thermodynamics of Quantum Information* (Morgan & Claypool Publishers, Kentfield, CA, 2019).
[14] K. Maruyama, F. Nori, and V. Vedral, Colloquium: The physics of Maxwell's demon and information, Rev. Mod. Phys. **81**, 1 (2009).
[15] M. O. Scully, Quantum photocell: Using quantum coherence to reduce radiative recombination and increase efficiency, Phys. Rev. Lett. **104**, 207701 (2010).
[16] X. L. Huang, T. Wang, and X. X. Yi, Effects of reservoir squeezing on quantum systems and work extraction, Phys. Rev. E **86**, 051105 (2012).
[17] F. Tonner and G. Mahler, Autonomous quantum thermodynamic machines, Phys. Rev. E **72**, 066118 (2005).
[18] W. Hao, S. Liu, and J. He, Thermal entanglement in two-atom cavity QED and the entangled quantum Otto engine, Phys. Rev. E **79**, 046409 (2009).
[19] H. P. Goswami and U. Harbola, Thermodynamics of quantum heat engines, Phys. Rev. A **88**, 013842 (2013).
[20] T. D. Kieu, The second law, Maxwell's demon, and work derivable from quantum heat engines, Phys. Rev. Lett. **93**, 140403 (2004).
[21] A. E. Allahverdyan, R. S. Gracia, and T. M. Nieuwenhuizen, Work extraction in the spin-Boson model, Phys. Rev. E **71**, 046106 (2005).
[22] J. Wang, Z. Wu, and J. He, Quantum Otto engine of a two-level atom with single-mode fields, Phys. Rev. E **85**, 041148 (2012).
[23] O. Abah, J. Rossnagel, G. Jacob, S. Deffner, F. Schmidt-Kaler, K. Singer, and E. Lutz, Single-ion heat engine at maximum power, Phys. Rev. Lett. **109**, 203006 (2012).
[24] J. Roßnagel, O. Abah, F. Schmidt-Kaler, K. Singer, and E. Lutz, Nanoscale heat engine beyond the Carnot limit, Phys. Rev. Lett. **112**, 030602 (2014).
[25] J. Roßnagel, S. T. Dawkins, K. N. Tolazzi, O. Abah, E. Lutz, F. Schmidt-Kaler, and K. Singer, A single-atom heat engine, Science **352**, 325 (2016).
[26] G. Maslennikov, S. Ding, R. Hablützel, J. Gan, A. Roulet, S. Nimmrichter, J. Dai, V. Scarani, and D. Matsukevich, Quantum absorption refrigerator with trapped ions, Nat. Commun. **10**, 202 (2019).
[27] K. Zhang, F. Bariani, and P. Meystre, Quantum optomechanical heat engine, Phys. Rev. Lett. **112**, 150602 (2014).
[28] K. Zhang, F. Bariani, and P. Meystre, Theory of an optomechanical quantum heat engine, Phys. Rev. A **90**, 023819 (2014).
[29] O. Fialko and D. Hallwood, Isolated quantum heat engine, Phys. Rev. Lett. **108**, 085303 (2012).
[30] J.-P. Brantut, C. Grenier, J. Meineke, D. Stadler, S. Krinner, C. Kollath, T. Esslinger, and A. Georges, A thermoelectric heat engine with ultracold atoms, Science **342**, 713 (2013).
[31] T. B. Batalhão, A. M. Souza, L. Mazzola, R. Auccaise, R. S. Sarthour, I. S. Oliveira, J. Goold, G. D. Chiara, M. Paternostro, and R. M. Serra, Experimental reconstruction of work distribution and study of fluctuation relations in a closed quantum system, Phys. Rev. Lett. **113**, 140601 (2014).
[32] K. Micadei, J. P. S. Peterson, A. M. Souza, R. S. Sarthour, I. S. Oliveira, G. T. Landi, T. B. Batalhão, R. M. Serra, and E. Lutz, Reversing the direction of heat flow using quantum correlations, Nat. Commun. **10**, 2456 (2019).
[33] R. J. de Assis, T. M. de Mendonça, C. J. Villas-Boas, A. M. de Souza, R. S. Sarthour, I. S. Oliveira, and N. G de Almeida, Efficiency of a quantum Otto heat engine operating under a reservoir at effective negative temperatures, Phys. Rev. Lett. **122**, 240602 (2019).
[34] H. T. Quan, Y. D. Wang, Y.-x. Liu, C. P. Sun, and F. Nori, Maxwell's demon assisted thermodynamic cycle in superconducting quantum circuits, Phys. Rev. Lett. **97**, 180402 (2006).

[35] A. O. Niskanen, Y. Nakamura, and J. P. Pekola, Information entropic superconducting microcooler, Phys. Rev. B **76**, 174523 (2007).

[36] J. P. Pekola, V. Brosco, M. Möttönen, P. Solinas, and A. Shnirman, Decoherence in adiabatic quantum evolution: Application to Cooper pair pumping, Phys. Rev. Lett. **105**, 030401 (2010).

[37] J. V. Koski, A. Kutvonen, I. M. Khaymovich, T. Ala-Nissila, and J. P. Pekola, On-chip Maxwell's demon as an information-powered refrigerator, Phys. Rev. Lett. **115**, 260602 (2015).

[38] J. P. Pekola, D. S. Golubev, and D. V. Averin, Maxwell's demon based on a single qubit, Phys. Rev. B **93**, 024501 (2016).

[39] T. Feldmann, E. Geva, R. Kosloff, and P. Salamon, Heat engines in finite time governed by master equations, Am. J. Phys. **64**, 485 (1996).

[40] T. Feldmann and R. Kosloff, Characteristics of the limit cycle of a reciprocating quantum heat engine, Phys. Rev. E **70**, 046110 (2004).

[41] Y. Rezek and R. Kosloff, Irreversible performance of a quantum harmonic heat engine, New J. Phys. **8**, 83 (2006).

[42] F. Tonner and G. Mahler, Quantum limit of the Carnot engine, Fortschr. Phys. **54**, 939 (2006).

[43] G. A. Barrios, F. Albarrán-Arriagada, F. J. Peña, E. Solano, and J. C. Retamal, Light-matter quantum Otto engine in finite time, arXiv:2102.10559.

[44] J. He, X. He, and W. Tang, The performance characteristics of an irreversible quantum Otto harmonic refrigeration cycle, Sci. China Ser. G: Phys. Mech. Astron. **52**, 1317 (2009).

[45] G. Thomas, M. Banik, and S. Ghosh, Implications of coupling in quantum thermodynamic machines, Entropy **19**, 442 (2017).

[46] G. Watanabe, B. P. Venkatesh, P. Talkner, and A. Del Campo, Quantum performance of thermal machines over many cycles, Phys. Rev. Lett. **118**, 050601 (2017).

[47] S. Hamedani Raja, S. Maniscalco, G. S. Paraoanu, J. P. Pekola, and N. L. Gullo, Finite-time quantum Stirling heat engine, New J. Phys. **23**, 033034 (2021).

[48] R. J. De Assis, J. S. Sales, U. C. Mendes, and N. G. de Almeida, Two-level quantum Otto heat engine operating with unit efficiency far from the quasi-static regime under a squeezed reservoir, J. Phys. B: At., Mol., Opt. Phys. **54**, 095501 (2021).

[49] T. Feldmann and R. Kosloff, Performance of discrete heat engines and heat pumps in finite time, Phys. Rev. E **61**, 4774 (2000).

[50] E. Geva and R. Kosloff, A quantum-mechanical heat engine operating in finite time. A model consisting of spin-1/2 systems as the working fluid, J. Chem. Phys. **96**, 3054 (1992).

[51] X. L. Huang, H. Xu, X. Y. Niu, and Y. D. Fu, A special entangled quantum heat engine based on the two-qubit Heisenberg xx model, Phys. Scr. **88**, 065008 (2013).

[52] X. L. Huang, Y. Liu, Z. Wang, and X. Y. Niu, Special coupled quantum otto cycles, Eur. Phys. J. Plus **129**, 4 (2014).

[53] E. A. Ivanchenko, Quantum Otto cycle efficiency on coupled qudits, Phys. Rev. E **92**, 032124 (2015).

[54] N. M. Myers and S. Deffner, Bosons outperform fermions: The thermodynamic advantage of symmetry, Phys. Rev. E **101**, 012110 (2020).

[55] N. M. Myers, O. Abah, and S. Deffner, Quantum otto engines at relativistic energies, New J. Phys. **23**, 105001 (2021).

[56] H. Wang, S. Liu, and J. He, Performance analysis and parametric optimum criteria of an irreversible Bose–Otto engine, J. Appl. Phys. **105**, 083534 (2009).

[57] N. M. Myers, F. J. Peña, O. Negrete, P. Vargas, G. De Chiara, and S. Deffner, Boosting engine performance with Bose–Einstein condensation, New J. Phys. **24**, 025001 (2022).

[58] F. Altintas, A. Ü. C. Hardal, and Ö. E. Müstecaplıoğlu, Rabi model as a quantum coherent heat engine: From quantum biology to superconducting circuits, Phys. Rev. A **91**, 023816 (2015).

[59] Q. Song, S. Singh, K. Zhang, W. Zhang, and P. Meystre, One qubit and one photon: The simplest polaritonic heat engine, Phys. Rev. A **94**, 063852 (2016).

[60] G. A. Barrios, F. Albarrán-Arriagada, F. A. Cárdenas-López, G. Romero, and J. C. Retamal, Role of quantum correlations in light-matter quantum heat engines, Phys. Rev. A **96**, 052119 (2017).

[61] B. Mojaveri, A. Dehghani, and Z. Ahmadi, A quantum correlated heat engine based on the parity-deformed Jaynes–Cummings model: Achieving the classical carnot efficiency by a local classical field, Phys. Scr. **96**, 115102 (2021).

[62] E. T. Jaynes and F. W. Cummings, Comparison of quantum and semiclassical radiation theories with application to the beam maser, Proc. IEEE **51**, 89 (1963).

[63] D. Braak, Integrability of the Rabi model, Phys. Rev. Lett. **107**, 100401 (2011).

[64] Q.-H. Chen, C. Wang, S. He, T. Liu, and K.-L. Wang, Exact solvability of the quantum Rabi model using Bogoliubov operators, Phys. Rev. A **86**, 023822 (2012).

[65] D. Braak, Q.-H. Chen, M. T. Batchelor, and E. Solano, Semiclassical and quantum rabi models: In celebration of 80 years, J. Phys. A: Math. Theor. **49**, 300301 (2016).

[66] I. I. Rabi, On the process of space quantization, Phys. Rev. **49**, 324 (1936).

[67] I. I. Rabi, Space quantization in a Gyrating magnetic field, Phys. Rev. **51**, 652 (1937).

[68] K. Hepp and E. H. Lieb, On the superradiant phase transition for molecules in a quantized radiation field: The dicke maser model, Ann. Phys. (NY) **76**, 360 (1973).

[69] Y. K. Wang and F. T. Hioe, Phase transition in the Dicke model of superradiance, Phys. Rev. A **7**, 831 (1973).

[70] M. Gross and S. Haroche, Superradiance: An essay on the theory of collective spontaneous emission, Phys. Rep. **93**, 301 (1982).

[71] M. Buchhold, P. Strack, S. Sachdev, and S. Diehl, Dicke-model quantum spin and photon glass in optical cavities: Nonequilibrium theory and experimental signatures, Phys. Rev. A **87**, 063622 (2013).

[72] P. Kirton and J. Keeling, Suppressing and restoring the Dicke superradiance transition by dephasing and decay, Phys. Rev. Lett. **118**, 123602 (2017).

[73] E. G. Dalla Torre, Y. Shchadilova, E. Y. Wilner, M. D. Lukin, and E. Demler, Dicke phase transition without total spin conservation, Phys. Rev. A **94**, 061802(R) (2016).

[74] J. Larson and E. K. Irish, Some remarks on superradiant phase transitions in light-matter systems, J. Phys. A: Math. Theor. **50**, 174002 (2017).

[75] Q.-H. Chen, Y.-Y. Zhang, T. Liu, and K.-L. Wang, Numerically exact solution to the finite-size Dicke model, Phys. Rev. A **78**, 051801(R) (2008).

[76] Q.-H. Chen, T. Liu, Y.-Y. Zhang, and K.-L. Wang, Quantum phase transitions in coupled two-level atoms in a single-mode cavity, Phys. Rev. A **82**, 053841 (2010).

[77] S. Schneider and G. J. Milburn, Entanglement in the steady state of a collective-angular-momentum (Dicke) model, Phys. Rev. A **65**, 042107 (2002).

[78] N. Lambert, C. Emary, and T. Brandes, Entanglement and the phase transition in single-mode superradiance, Phys. Rev. Lett. **92**, 073602 (2004).

[79] E. Wolfe and S. F. Yelin, Certifying separability in symmetric mixed states of *N* qubits, and superradiance, Phys. Rev. Lett. **112**, 140402 (2014).

[80] C. Emary and T. Brandes, Quantum chaos triggered by precursors of a quantum phase transition: The Dicke model, Phys. Rev. Lett. **90**, 044101 (2003).

[81] P. Kirton and J. Keeling, Superradiant and Lasing states in driven-dissipative Dicke models, New J. Phys. **20**, 015009 (2018).

[82] L. Fusco, M. Paternostro, and G. D. Chiara, Work extraction and energy storage in the Dicke model, Phys. Rev. E **94**, 052122 (2016).

[83] C. Ciuti, G. Bastard, and I. Carusotto, Quantum vacuum properties of the intersubband cavity polariton field, Phys. Rev. B **72**, 115303 (2005).

[84] G. Günter, A. A. Anappara, J. Hees, A. Sell, G. Biasiol, L. Sorba, S. D. Liberato, C. Ciuti, A. Tredicucci, A. Leitenstorfer *et al.*, Sub-cycle switch-on of ultrastrong light–matter interaction, Nature (London) **458**, 178 (2009).

[85] T. Niemczyk, F. Deppe, H. Huebl, E. P. Menzel, F. Hocke, M. J. Schwarz, J. J. Garcia-Ripoll, D. Zueco, T. Hümmer, E. Solano *et al.*, Circuit quantum electrodynamics in the ultrastrong-coupling regime, Nat. Phys. **6**, 772 (2010).

[86] P. Forn-Díaz, J. Lisenfeld, D. Marcos, J. J. Garcia-Ripoll, E. Solano, C. J. P. M. Harmans, and J. E. Mooij, Observation of the Bloch-Siegert shift in a qubit-oscillator system in the ultrastrong coupling regime, Phys. Rev. Lett. **105**, 237001 (2010).

[87] A. Zazunov, V. S. Shumeiko, E. N. Bratus, J. Lantz, and G. Wendin, Andreev level qubit, Phys. Rev. Lett. **90**, 087003 (2003).

[88] C. Janvier, L. Tosi, L. Bretheau, Ç. Ö. Girit, M. Stern, P. Bertet, P. Joyez, D. Vion, D. Esteve, M. F. Goffman *et al.*, Coherent manipulation of Andreev states in superconducting atomic contacts, Science **349**, 1199 (2015).

[89] T. Schwartz, J. A. Hutchison, C. Genet, and T. W. Ebbesen, Reversible switching of ultrastrong light-molecule coupling, Phys. Rev. Lett. **106**, 196405 (2011).

[90] A. J. Hoffman, S. J. Srinivasan, S. Schmidt, L. Spietz, J. Aumentado, H. E. Türeci, and A. A. Houck, Dispersive photon blockade in a superconducting circuit, Phys. Rev. Lett. **107**, 053602 (2011).

[91] G. Scalari, C. Maissen, D. Turčinková, D. Hagenmüller, S. D. Liberato, C. Ciuti, C. Reichl, D. Schuh, W. Wegscheider, M. Beck *et al.*, Ultrastrong coupling of the cyclotron transition of a 2D electron gas to a thz metamaterial, Science **335**, 1323 (2012).

[92] A. L. Boité, M.-J. Hwang, H. Nha, and M. B. Plenio, Fate of photon blockade in the deep strong-coupling regime, Phys. Rev. A **94**, 033827 (2016).

[93] A. Settineri, V. Macrí, A. Ridolfo, O. Di Stefano, A. F. Kockum, F. Nori, and S. Savasta, Dissipation and thermal noise in hybrid quantum systems in the ultrastrong-coupling regime, Phys. Rev. A **98**, 053834 (2018).

[94] F. Beaudoin, J. M. Gambetta, and A. Blais, Dissipation and ultrastrong coupling in circuit QED, Phys. Rev. A **84**, 043832 (2011).

[95] T. Ye, C. Wang, and Q.-H. Chen, Quantum phase transition of light in the dissipative Rabi-Hubbard lattice: A dressed-master-equation perspective, Phys. Rev. A **104**, 053708 (2021).

[96] C. W. Gardiner and M. J. Collett, Input and output in damped quantum systems: Quantum stochastic differential equations and the master equation, Phys. Rev. A **31**, 3761 (1985).

[97] R. J. de Assis, J. S. Sales, J. A. R. da Cunha, and N. G. de Almeida, Universal two-level quantum Otto machine under a squeezed reservoir, Phys. Rev. E **102**, 052131 (2020).

[98] R. H. Dicke, Coherence in spontaneous radiation processes, Phys. Rev. **93**, 99 (1954).

[99] P. Kirton, M. M. Roses, J. Keeling, and E. G. D. Torre, Introduction to the Dicke model: From equilibrium to nonequilibrium, and vice versa, Adv. Quantum Technol. **2**, 1970013 (2019).

[100] A. Solfanelli, M. Falsetti, and M. Campisi, Nonadiabatic single-qubit quantum Otto engine, Phys. Rev. B **101**, 054513 (2020).

[101] R. J. Glauber, The quantum theory of optical coherence, Phys. Rev. **130**, 2529 (1963).

[102] P. Rabl, Photon blockade effect in optomechanical systems, Phys. Rev. Lett. **107**, 063601 (2011).

[103] A. Ridolfo, M. Leib, S. Savasta, and M. J. Hartmann, Photon blockade in the ultrastrong coupling regime, Phys. Rev. Lett. **109**, 193602 (2012).

[104] J. Eisert and M. B. Plenio, A comparison of entanglement measures, J. Mod. Opt. **46**, 145 (1999).

[105] K. Życzkowski, P. Horodecki, A. Sanpera, and M. Lewenstein, Volume of the set of separable states, Phys. Rev. A **58**, 883 (1998).

[106] M. Kitagawa and M. Ueda, Squeezed spin states, Phys. Rev. A **47**, 5138 (1993).

[107] T. R. de Oliveira and D. Jonathan, Efficiency gain and bidirectional operation of quantum engines with decoupled internal levels, Phys. Rev. E **104**, 044133 (2021).

[108] A. E. Makouri, A. Slaoui, and M. Daoud, Enhancing the performance of coupled quantum otto thermal machines without entanglement and quantum correlations, J. Phys. B: At., Mol., Opt. Phys. **56**, 085501 (2023).

[109] Z. Zhiqiang, C. H. Lee, R. Kumar, K. J. Arnold, S. J. Masson, A. S. Parkins, and M. D. Barrett, Nonequilibrium phase transition in a spin-1 Dicke model, Optica **4**, 424 (2017).

[110] A. T. Black, H. W. Chan, and V. Vuletić, Observation of collective friction forces due to spatial self-organization of atoms: From Rayleigh to Bragg scattering, Phys. Rev. Lett. **91**, 203001 (2003).

[111] A. Safavi-Naini, R. J. Lewis-Swan, J. G. Bohnet, M. Gärttner, K. A. Gilmore, J. E. Jordan, J. Cohn, J. K. Freericks, A. M. Rey, and J. J. Bollinger, Verification of a many-ion simulator of the Dicke model through slow quenches across a phase transition, Phys. Rev. Lett. **121**, 040503 (2018).

[112] P. Pietzonka and U. Seifert, Universal trade-off between power, efficiency, and constancy in steady-state heat engines, Phys. Rev. Lett. **120**, 190602 (2018).

[113] S. Mohanta, M. Saha, B P. Venkatesh, and B. K. Agarwalla, Bounds on nonequilibrium fluctuations for asymmetrically driven quantum Otto engines, Phys. Rev. E **108**, 014118 (2023).

[114] S. Saryal and B. K. Agarwalla, Bounds on fluctuations for finite-time quantum Otto cycle, Phys. Rev. E **103**, L060103 (2021).

[115] S. Mohanta and B. K. Agarwalla, Full statistics of non-equilibrium heat and work for many-body quantum Otto engine and universal bounds: A non-equilibrium Green's function approach, Phys. Rev. E **108**, 064127 (2023).